Proceedings of ICFDP9
Ninth International Congress of Fluid Dynamics & Propulsion
December 18-21, 2008, Alexandria, Egypt

ICFDP9-EG-241

OPTIMUM SIZING OF TWO DISKS ARRANGED IN TANDEM PLACED NORMAL TO A TURBULENT FLOW

Richard J. M. Messiha
rjmessiha@asunet.shams.edu.eg

Mohamed S. El-Morsi
melmorsi@asunet.shams.edu.eg

Mechanical Power Engineering Dept.
Ain Shams University, Cairo 11517, Egypt

ABSTRACT

Steady-state simulations are presented for the axisymmetric flow over two circular thin disks arranged in tandem and placed normal to a turbulent flow. Computations are performed at a value of 4×10^4 for the Reynolds number of the undisturbed oncoming flow, based on the reference disk diameter. The performance of three turbulent closure models in conjunction with a finite-volume-based numerical prediction procedure was tested. These are the standard k-ε, the RNG k-ε and the Reynolds stress models. The results obtained using the standard k-ε model under-predict the optimum spacing between the two disks, while those of the Reynolds stress model over-predict this spacing. Numerical results of the RNG k-ε model indicate a reasonable agreement with the available experimental measurements concerning both the percentage of drag reduction and the optimum gap.

1. INTRODUCTION

One of the more interesting topics in bluff-body aerodynamics is the interaction of two bluff bodies placed in tandem. The interesting aspect of this topic is that the flow pattern and drag of a tandem configuration cannot be easily predicted from the known flow characteristics of the two individual bodies that form it. The reason for this is that the rear body is exposed to a flow perturbed and substantially altered by the front body and, in addition, there is also some upstream influence of the rear body on the front-body flow field. There are many examples of flows over bodies in tandem that one can identify in our every day experience. For example, flow around two or more neighboring buildings. The other possible example would be the flow past vehicles, e.g. trucks traveling one behind the other and the tractor-trailer combinations one can see on the road.

In the case of neighboring buildings the bodies are not directly connected, and one is interested only in the changes in the flow field of one building as it is affected by the presence of its neighbours. The distribution of air may cause the transport of auto-emissions, dust, etc., into the buildings. In cases like that of tractor-trailers, the bodies are directly connected and one is interested in the flow field of, and forces acting on, the entire system of the connected bodies, as well.

Modification and control of the bluff-body wake flow can be employed either, to intensify turbulence in the wake flow in order to enhance heat transfer, mixing and combustion or, to reduce the intensity of turbulence in the wake in order to reduce drag. Placing two bluff bodies, two disks or a disk and a cylinder, in tandem is known to lead to configurations with relatively lower overall drag than a single body.

The case of two disks of equal diameters placed in tandem was studied some 90 years ago by Eiffel [1]. His results showed that the combination of two disks separated by not too large gap produces a smaller drag than a single disk alone. It was striking to notice that the rear disk experienced a negative drag force (acting forward) over a wide range of axial-gap/diameter ratio < 2.26.

Another related experiment is that of Roshko and Koenig [2], who investigated the effect of diameter ratio and gap length on the drag of a flat-faced circular cylinder preceded by a concentric circular disk. They found that one optimal configuration, with disk-to-cylinder diameter ratio of 0.75 and gap-to-cylinder diameter ratio of 0.375, produced an impressive drag reduction from 0.75 to 0.02, i.e., close to the pressure-drag coefficient in the case of potential flow around a body.

Experimental study of Morel and Bohn [3] with two disks of different diameters placed in tandem and connected together showed that very significant drag reduction may be achieved by proper sizing of the disks diameters and the axial gap between them. Their study led to the identification of four different operating regimes, depending on the ratio of the front to rear disk diameters D_1 / D_2. Among them, the most important is the regime where D_1 / D_2 lies between 0.65 and 0.8, at which the most significant drag reduction was observed at a gap length L around $0.5D_2$. By choosing $D_1 / D_2 = 0.8$ and $L / D_2 = 0.54$, they reported a total drag reduction of 0.81.

Selim [4] concluded, as a result of his experimental measurements, for tandem disks of equal diameters that a maximum drag reduction of 0.21 occurred at a value approximately equal to 1.33 for the ratio of the separation distance to disk diameter. He reported also that at a separation distance greater than three diameters, the system of tandem disks behaves as two individual disks.

Since proper sizing of the disks diameters and the gap between them is crucial to the drag reduction, and since available information on the velocity and turbulence characteristics of wake flows with recirculation is limited for the tandem disks configuration. Therefore, the present investigation was motivated by the desire to extend the knowledge of the aerodynamic characteristics of axisymmetric turbulent wake flows behind tandem disks.

The present study is concerned with the steady-state simulation for the axisymmetric turbulent flow over two circular thin disks, each of thickness t, arranged in tandem and placed normal to the flow. The flow characteristics are investigated for geometrical configurations of the two disks having either equal or unequal diameters and covering a significant range of the gap between them. For the objective of drag reduction, the present study is concerned with the determination of the optimum ratio of the axial-gap to reference-disk diameter L / D_2 as well as its dependence on the ratio of the disks diameters D_1 / D_2.

2. MATHEMATICAL FORMULATION

The Reynolds-averaged Navier-Stokes (RANS) equations can be written for incompressible, steady, isothermal, swirl-free axisymmetric flow in the cylindrical coordinates as follows:

The continuity equation

$$\frac{\partial U}{\partial x}+\frac{1}{r}\frac{\partial (rV)}{\partial r}=0 \tag{1}$$

The momentum equations

$$U\frac{\partial U}{\partial x}+V\frac{\partial U}{\partial r}=-\frac{1}{\rho}\frac{\partial P}{\partial x}+\nu\left[\frac{\partial^2 U}{\partial x^2}+\frac{1}{r}\frac{\partial}{\partial r}\left(r\frac{\partial U}{\partial r}\right)\right]-\frac{\partial \overline{u^2}}{\partial x}-\frac{1}{r}\frac{\partial (r\overline{uv})}{\partial r} \tag{2}$$

$$U\frac{\partial V}{\partial x}+V\frac{\partial V}{\partial r}=-\frac{1}{\rho}\frac{\partial P}{\partial r}+\nu\left[\frac{\partial^2 V}{\partial x^2}+\frac{\partial}{\partial r}\left(\frac{1}{r}\frac{\partial (rV)}{\partial r}\right)\right]-\frac{\partial \overline{uv}}{\partial x}-\frac{1}{r}\frac{\partial (r\overline{v^2})}{\partial r}+\frac{\overline{w^2}}{r} \tag{3}$$

In the above equations, the upper case denotes ensemble-mean quantities for the velocity components U and V and for the static pressure P. ρ is the fluid density and ν is the fluid kinematic viscosity. The single-point correlation terms $\overline{u_i u_j}$ represent the turbulent or Reynolds stresses given by $\tau_{ij}=-\rho\overline{u_i u_j}$, where the axes in the directions x, r, θ are labeled 1, 2, 3 respectively.

The momentum equations are not a closed set and turbulence models are needed. The linear k-ε and Reynolds stress models, used in the present study, are now defined.

2.1 Linear two-equation models

In the linear k-ε models the stress-strain relation is defined as follows:

$$-\overline{u_i u_j}=2\nu_t S_{ij}-\frac{2}{3}\delta_{ij}k \tag{4}$$

where ν_t is the eddy or turbulent kinematic viscosity, $k=\frac{1}{2}\overline{u_i u_i}$ is the turbulence kinetic energy and δ_{ij} is the Kronecker delta (= 1 for i = j and = 0 for i ≠ j). S_{ij} is regarded as the fluid mean rate of strain tensor whose elements, in axisymmetric coordinates, are:

$$S_{xx}=\frac{\partial U}{\partial x},\ S_{rr}=\frac{\partial V}{\partial r},\ S_{\theta\theta}=\frac{V}{r}\ \text{and}\ S_{xr}=\frac{1}{2}\left(\frac{\partial U}{\partial r}+\frac{\partial V}{\partial x}\right) \tag{5}$$

The eddy viscosity used in the k-ε models is defined by the following expression:

$$\nu_t=C_\mu k^2/\varepsilon \tag{6}$$

with the coefficient C_μ given in Table 1 (for the various models used). ε is the dissipation rate of k defined as:

$$\varepsilon=\nu\overline{\left(\frac{\partial u_i}{\partial x_m}\right)^2} \tag{7}$$

The values of the scalar quantities k and ε needed to calculate ν_t are determined from the following modeled transport equations:

$$U\frac{\partial k}{\partial x}+V\frac{\partial k}{\partial r}=\frac{\partial}{\partial x}\left(\Gamma_k\frac{\partial k}{\partial x}\right)+\frac{1}{r}\frac{\partial}{\partial r}\left(r\Gamma_k\frac{\partial k}{\partial r}\right)+G-\varepsilon \tag{8}$$

$$U\frac{\partial \varepsilon}{\partial x}+V\frac{\partial \varepsilon}{\partial r}=\frac{\partial}{\partial x}\left(\Gamma_\varepsilon\frac{\partial \varepsilon}{\partial x}\right)+\frac{1}{r}\frac{\partial}{\partial r}r\left(\Gamma_\varepsilon\frac{\partial \varepsilon}{\partial r}\right)+C_{\varepsilon 1}G\frac{\varepsilon}{k}-C_{\varepsilon 2}\frac{\varepsilon^2}{k}-C_{\varepsilon 3}R_\varepsilon \tag{9}$$

where Γ_ϕ is the diffusion coefficient of the variable ϕ and G is the turbulent kinetic energy production rate given by:

$$G = -\overline{u_i u_j}\, S_{ij} \tag{10}$$

Two of the most widely used linear models is the standard model by Launder and Spalding [5], LS, and the RNG-based model by Yakhot et al. [6 and 7], RNG. The models constants σ_k, σ_ε, $C_{\varepsilon 1}$, $C_{\varepsilon 2}$ and $C_{\varepsilon 3}$ are given also in Table 1. In the standard k-ε model $\Gamma_\phi = \nu + \nu_t/\sigma_\phi$, while in the RNG-based model $\Gamma_\phi = (\nu + \nu_t)/\sigma_\phi$. The extra term, R_ε, appearing in the RNG formulation, is calculated as follows:

$$R_\varepsilon = \frac{C_\mu \eta^3 (1 - \eta/\eta_o)}{1 + \beta\eta^3} \frac{\varepsilon^2}{k} \tag{11}$$

where the parameter $\eta = k\sqrt{2S_{ij}S_{ij}}\,/\varepsilon$ is the dimensionless strain invariant. The other model constants are $\eta_o = 4.38$ and $\beta = 0.012$.

Table 1: Constants for the standard and RNG linear models.

	C_μ	σ_k	σ_ε	$C_{\varepsilon 1}$	$C_{\varepsilon 2}$	$C_{\varepsilon 3}$
LS [5]	0.09	1.0	1.3	1.44	1.92	0.0
RNG[6, 7]	0.0845	0.7197	0.7197	1.42	1.68	1.0

2.2 Reynolds stress model

The Reynolds stress model, RMS, involves the calculation of the individual Reynolds stresses, $\overline{u_i u_j}$, using the differential transport equations. Referring to Gatski [8], these equations may be written in the following form:

$$U\frac{\partial \overline{u_i u_j}}{\partial x} + V\frac{\partial \overline{u_i u_j}}{\partial r} = P_{ij} + \Pi_{ij} + T_{ij} + L_{ij} - \varepsilon_{ij} \tag{12}$$

where P_{ij} is the turbulent production, Π_{ij} is pressure strain rate, T_{ij} is the turbulent diffusion, L_{ij} is the molecular diffusion and ε_{ij} is the turbulent dissipation rate. It is worth noting that $G = \frac{1}{2}P_{ii}$ and $\varepsilon = \frac{1}{2}\varepsilon_{ii}$. For the coordinate system under consideration, the detailed Reynolds-stress equations are given in Appendix A.

Of the terms of Eq. (12) the turbulent production and the molecular diffusion can be treated exactly. However, Π_{ij}, T_{ij} and ε_{ij} need to be modeled to close the equations. The pressure strain rate Π_{ij} is modeled by the linear pressure-strain model proposed by Launder [9]. The turbulent diffusion term T_{ij} is modeled by the simplified gradient-diffusion model of Lien and Leschziner [10]. The turbulent dissipation rate ε_{ij} is modeled as

$$\varepsilon_{ij} = \tfrac{2}{3}\delta_{ij}\varepsilon \tag{13}$$

and the scalar dissipation rate, ε, is computed with the model transport equation (9).

2.3 Boundary Conditions

For the flow geometry under consideration, the computational domain boundaries, shown in Fig. 1, were set as follows:

i) At the inlet boundary (AB), uniform flow conditions are imposed for all variables using the available experimental inlet conditions:

$$U = U_o,\ V = 0,\ k = k_o \text{ and } \varepsilon_o = k_o^{3/2}/(\lambda W) \tag{14}$$

where k_o is specified to correspond to a uniform isotropic turbulence intensity $I = \sqrt{\frac{2}{3}k}/U_o$ lower than 0.1. Following the recommendation of Cebeci et al. [11], a value of λ = 0.005 is prescribed, where W is the wind tunnel width.

ii) Along the symmetry axis (AD), a zero cross-stream gradient condition, $\partial(\ )/\partial r$, is specified for all variables with V = 0.

iii) The no-slip boundary conditions are imposed along solid boundaries (BC, EF, FG, GH, IJ, JK and KL). According to Launder and Spalding [5], and in the absence of better information, the diffusion of k to the wall is set equal to zero, or $\partial k/\partial y = 0$. The near-wall values of the parallel velocity component, the turbulent kinetic energy and its dissipation rate are specified by the wall shear stress based on the wall-function approach [5]. This approach is usually used to bridge the gap between the fully turbulent region and the wall. In the derivation of the wall function, y^+ and U^+ are taken as the nondimensional normal distance and resultant velocity parallel to the wall, respectively, defined as

$$y^+ = yU_\tau/\nu,\ U^+ = U_{res}/U_\tau \text{ where } U_\tau = \sqrt{\tau_w/\rho} \tag{15}$$

In the equilibrium layer near the wall, the production of k is in balance with its dissipation rate. Assuming that the dominant term in the near wall production of k is that resulting from the shear stress, which is nearly constant, the following expression can be derived using Eqs. (4, 6, 8 & 10).

$$\tau_w = C_\mu^{1/2}\rho k \tag{16}$$

The dimensionless velocity parallel to the wall is calculated from the universal velocity profile,

$$U^+ = y^+ \qquad \text{for the viscous layer } (y^+ < 11.63) \tag{17a}$$

$$U^+ = \frac{1}{\kappa}\ln\left(Ey^+\right) \qquad \text{in the fully turbulent region } (y^+ > 11.63) \tag{17b}$$

where von Karman constant κ and E are the log-law constants and equal to 0.4187 and 9.793, respectively.

Using Eqs. (10 & 17b), the near wall production of k can be represented as follows:

$$G = U_\tau^3/(\kappa y) \tag{18}$$

The production of k for a given finite volume that lies immediately adjacent to the wall is obtained by integrating Eq. (18) over the region occupied by the node P next to the wall. Based on the assumption that the flow is in local equilibrium in the near wall region, $\varepsilon = G$, the value of ε at y_P is simply expressed as

$$\varepsilon_P = U_\tau^3/(\kappa y_P) \tag{19}$$

Equation (19) replaces the transport equation for ε, namely Eq. (9), at the nodes that lie immediately adjacent to the wall.

iv) The outlet boundary (CD) is positioned at a location where for all grid points next to it the Peclet number is sufficiently large. In this case the region near the outflow boundary exhibits a local one-way behaviour. In other words the value of a variable at any point will be uninfluenced by any of the downstream values.

3. COMPUTATIONAL DETAILS

3.1 Numerical Model

A control-volume formulation is used to derive algebraic approximations to the set of governing elliptic partial differential equations with the associated boundary conditions. The control-volume technique consists of integrating the differential equations about each control volume yielding discrete equations that conserve each quantity. A staggered nonuniform grid arrangement, with velocity nodes offset from scalar nodes, is used in the present computations. The grid layout adopted has centered volume faces in which the control volume faces are placed midway between the grid points. The discretization scheme used for the diffusion terms is the central difference. The face values required for the convection terms must be interpolated from the cell centre values. This is accomplished using the second-order upwind scheme. In this scheme the face values are determined by unidirectional extrapolation from two nodal points values on the upwind side of the face point in question.

The domain of solution considered is extended upstream the front disk to a distance of $10D_2$, to a downstream distance of $15D_2$ from the rear disk and to a lateral dimension of $10D_2$. The locations of these boundaries were determined after several computations to insure that they have no noticeable effect on the flow in the recirculation region. A proper resolution of the region immediately around the disk was found particularly critical to the accuracy of the solution. Consequently, a cluster of fine grids was located at this region with minimum grid size of $0.016D_2$ for either Δx_{min} or Δr_{min}.

To minimize the truncation errors associated with nonuniform grid distribution, the effect of the grid expansion factors $E_x = \Delta x_i / \Delta x_{i-1}$ and $E_r = \Delta r_j / \Delta r_{j-1}$ was investigated. It was found that a reliable solution could be obtained, without loss of accuracy, if these expansion factors are kept within the following ranges, where x is the axial distance measured from the front disk.

$$0.8 \le E_x, E_r \le 1.2 \text{ for} \begin{cases} -1 \ge x/D_1 \text{ and } (x-L)/D_2 \ge 3 \\ r/D_2 \ge 1 \end{cases} \tag{20}$$

otherwise

$$0.9 \le E_x, E_r \le 1.1 \tag{21}$$

3.2 Solution Procedure

The set of difference equations were solved iteratively using the solution algorithm outlined by Patankar [12], incorporating the semi-implicit method for pressure-linked equations. The code uses a line-by-line solution procedure which is a combination of the tridiagonal matrix solver and Gauss-Seidel technique. Underrelaxation factors were used to promote stability with values of 0.7, 0.7, 0.8 and 0.8 for U, V, k and ε, respectively. The pressure correction field was underrelaxed with a value of 0.3, whereas no relaxation was applied to the turbulent viscosity field.

It should be noted that the value of k at the node P immediately adjacent to the wall, k_P, is calculated from the regular balance equation for k, Eq. (8), in each iteration step. Such value of k_P is necessary to assign a value for y_P^+ via Eqs. (15 & 16). Since the k-ε model is only valid in the fully turbulent region, care has to be taken to ensure that the first grid line adjacent to the wall lies at a distance $y_P^+ > 11.63$ where Eq. (17b) is applied. If during the iteration process the value of y_P^+ drops below 11.63, Eq. (17a) is employed.

The mesh size was determined by conducting a grid independence study on the solution. Grid independence was established by examining the cross-stream velocity distributions at the middle of the recirculation zone. For this purpose, Reynolds number, Re,

was chosen to be 4×10^4 and for the same expansion factors, a number of different uniform and nonuniform grid distributions were investigated. Grid independence was attained when maximum changes in velocity distribution were less than 1 %.

The iteration cycle is terminated and the solution is considered converged, when the scaled residuals of the mass, momentum and turbulence quantities reach a value of less than 10^{-6}. The scaled residual, for any variable, is obtained by the summation of the residuals over all the computational cells and normalization using the flow rate of the variable through the domain. For a typical (880×370) grid, each run required about 3500 iterations to reach a converged solution.

4. RESULTS AND DISCUSSION

4.1 Preliminary Computations

Preliminary computations were performed in order to assess the capability of the selected turbulence models to predict the flow field around tandem disks. Namely, these are the standard model, LS, the RNG-based model, RNG and the Reynolds stress model, RMS. All of the numerical predictions presented in this and the subsequent sections were obtained at a value of Reynolds number, $Re = 4 \times 10^4$. Obviously, the drag coefficient was chosen to be the coefficient of interest and judgment was based according to it. The present predictions are compared with available experimental measurements from several sources. The drag coefficient is defined as follows:

$$C_D = F_D \Big/ \left(\frac{1}{2} \rho U_0^2 A \right) \tag{22}$$

where A is the projected area of the reference disk normal to the flow and the drag force is computed by performing the following integrals:

$$F_D = \int_{C.S} [P \cos(\hat{n}, x) + \tau_w \cos(\hat{s}, x)] dS \tag{23}$$

and n and s are the inward normal and the tangential direction to the surface S.

It is well established fact that measurements made in a wind tunnel whose test section is bounded by solid walls do not duplicate exactly a free-stream unbounded environment. This is a consequence of the constraining effect of the tunnel walls which makes the near-wall streamlines follow the wall contours, rather than being shaped by the flow field around the tested model. This constraining effect is felt at the model itself and results in a modification of the local flow field around it. The smaller the model frontal area, as compared to the tunnel cross-sectional area (model blockage), the weaker is the constraining effect of the tunnel walls. This effect and its magnitude have been the subject of many studies. One of the best known is the analysis performed by Maskell [14]. This analysis is often being applied to a broad range of bluff-body geometries. Therefore, when Maskell's analysis is applied to the present configuration it results in a correction factor of 0.9925 for the drag coefficient.

The first configuration studied was obviously that of a single disk. Its drag coefficient was computed using LS, RNG and RSM turbulence models and compared with the available published experimental data whose average value is 1.13. The result of this comparison is given in Table 2. It can be concluded that computations using RNG turbulence model predict the value of C_D more accurately than the other tested two models.

Table 2: Drag coefficient for a single disk.

Present Computations	Experimental Data

LS [5]	RNG [6&7]	RSM [8,9&10]	Ref. [1]	Ref. [3]	Ref. [4]	Ref. [15]	Ref. [16]	Ref. [17]
1.184	1.119	1.184	1.12	1.148	1.125	1.12	1.1	1.17

4.2 Two Disks of Equal Diameter

The present section is concerned with the study of the effect, on the drag, of varying the axial gap length L between two thin disks of equal diameter $D_1 = D_2$ placed in tandem. The results of this study are obtained using the three tested turbulence models, mentioned earlier, and are plotted in Fig. 2. For comparison, the data of Eiffel [1], Morel and Bohn [3] and Selim [4] are included in the same figure. All data, including the present, are seen to be quite similar in shape, but there is a consistent shift between them. The cause of this shift may result either from the difference in model blockage, in Re, or in the free-stream turbulence level. Any of these possibilities would introduce an additional parameter into the problem, so a closer look might be needed to sort out the reasons for the differences between the results. However, this aspect of the problem was considered outside the scope of the present study.

The drag coefficient is based on the total drag acting on both disks. Figure 2 shows that the drag coefficient C_D of the system has a quite interesting behaviour. First, C_D decreased with increasing the gap, then reaching a minimum around $L/D_2 = 1.5$ and finally it increased going toward its limiting value of twice that of the single disk. From the examination of the numerical results plotted in Fig. 2, one may conclude that the results obtained using the standard k-ε model, LS, under-predict the optimum spacing between the two disks, while those of the Reynolds stress model, RSM, over-predict this spacing. Numerical results of the RNG k-ε model indicate a reasonable agreement with the available experimental measurements concerning both the percentage of drag reduction and the optimum gap.

4.3 Two Disks of Unequal Diameter

All the data presented in this section were obtained using the RNG turbulence model. As mentioned above the drag coefficient is based on the total drag acting on both disks and is referred to the area of the rear disk having diameter D_2.

Figure 3 shows the drag coefficient C_D as obtained numerically for 4 values of D_1/D_2, namely 0.7, 0.9, 1.0 and 1.1. All four curves have the same general behaviour, which is the same as that described already in the previous section. C_D first decreases with increasing the gap, then reaches a minimum and followed by an increase. However it appears some distinct behaviours for each of them.

The curve for $D_1/D_2 = 0.7$ is very smooth, and experienced the lowest drag reaching a minimum of 0.287 at $L/D_2 = 0.5$. The curve for $D_1/D_2 = 0.9$ differs by a distinguishing feature: a smooth decrease at small gap lengths followed by a much less smooth behaviour reaching a minimum of 0.478 at $L/D_2 = 1.0$. The curve for $D_1/D_2 = 1.0$ shows the same trend but with less steep behaviour reaching a minimum of 0.732 at $L/D_2 = 1.45$. While the curve for $D_1/D_2 = 1.1$ shows the same behaviour as that for $D_1/D_2 = 1.0$ but reaches a minimum of 0.997 at $L/D_2 = 1.8$.

The salient point on each of the curves is that the minimum drag $(C_D)_{min}$ occurs at one optimum gap length $(L/D_2)_{opt}$. The dependence of $(C_D)_{min}$ and $(L/D_2)_{opt}$ on the ratio D_1/D_2 is summarized in Table 3.

Table 3: Drag coefficient for two disks in tandem.

D_1/D_2	0.7	0.9	1.0	1.1
$(L/D_2)_{opt}$	0.5	1.0	1.45	1.8
$(C_D)_{min}$	0.287	0.478	0.732	0.997

Figures 4 to 7 present comparison between the present numerical predictions using the RNG turbulence model with the available published experimental data of Eiffel [1], Morel and Bohn [3] and Selim [4]. The comparison results in a maximum error of 15% for the configuration with $D_1/D_2 = 0.7$, 36% for the case of $D_1/D_2 = 0.9$, 15% for the case of $D_1/D_2 = 1.0$ and 13% for the case of $D_1/D_2 = 1.1$. For the configuration with $D_1/D_2 = 0.9$, Morel and Bohn [3] reported that the flow became unsteady and produced model vibration. This could the reason for the relatively high error occurring in this case.

Figures 8 to 10 give the mean streameline representation for the flow field past tandem configurations with $D_1/D_2 = 0.7$, 0.9 and 1.1, respectively. One can observe that the upstream shear layer almost reattaches on the trailing edge of the downstream body and the gap vortex is formed. For shorter spacings, the flow always overshoots, whereas for longer spacings the shear layer rolls into the gap. It was observed also, from the numerical computations results, that the turbulence intensities were significantly reduced in the wake regions of the configurations corresponding to the minimum values of the drag coefficients, see Figs. 8b, 9b and 10b. This fact coincides with the proposed reason for the drag reduction in such tandem configurations.

5. CONCLUSIONS

Numerical predictions of the steady-state simulation for the axisymmetric turbulent flow over two circular thin disks arranged in tandem and placed normal to the flow showed that a significant drag reduction from that of a single disk may be achieved by proper sizing of the disk diameters and the axial gap between them. Further study is required to cover all the ranges of D_1/D_2 and L/D_2 in order to identify clearly the optimum size for the tandem disks configuration.

The standard k-ε and Reynolds stress models failed to represent the effects of turbulence in the flow presently examined. The RNG turbulence-model, accounting for the effects of streamline curvature, lead to improved agreement with the experimental data concerning both the percentage of drag reduction and the optimum gap length.

.

NOMENCLATURE

Symbol Definition

A	frontal area of the reference disk normal to the flow
C_D	drag coefficient $\left[=F_D\Big/\left(\frac{1}{2}\rho U_o^2 A\right)\right]$
$C_{\varepsilon 1}, C_{\varepsilon 2}, C_{\varepsilon 3}$	empirical constants used in the two-equation k-ε model
C_μ	empirical constant in Eq. (6)
D_1, D_2	diameters of the front and rear disks, respectively
E	constant in the logarithmic law of the wall, Eq. (17b)
F_D	drag force
G	production rate of turbulence kinetic energy $\left(=-\overline{u_i u_j}\,S_{ij}\right)$
I	isotropic turbulence intensity $\left(=\sqrt{\frac{2}{3}k}\Big/U_o\right)$
k	turbulence kinetic energy $\left(=\frac{1}{2}\overline{u_i u_i}\right)$
L	axial gap length between the two disks
L_{ij}	molecular diffusion term of Reynolds stress model
P	time-mean static pressure
P_{ij}	turbulent production term of Reynolds stress model
r, x	radial and axial coordinates
Re	Reynolds number $\left(=U_o D/\nu\right)$
R_ε	extra term appearing in the RNG formulation, Eq. (11)
S_{ij}	fluid mean rate of strain tensor, Eq. (5)
t	disk thickness
T_{ij}	turbulent diffusion term of Reynolds stress model
u_i	fluctuating velocity components
U, V	axial and radial time-mean velocity components
$U_s,\ U^+$	dimensional and dimensionless resultant velocity parallel to the wall $\left(U^+ = U_s/U_\tau\right)$
U_τ	shear velocity $\left(=\sqrt{\tau_w/\rho}\right)$
W	wind tunnel width
$y,\ y^+$	dimensional and dimensionless normal distance to the wall $\left(y^+ = yU_\tau/\nu\right)$

Greek letters

δ_{ij}	Kronecker delta $\left(=1 \text{ for } i=j \text{ and } =0 \text{ for } i\neq j\right)$
$\Delta r,\ \Delta x$	internodal distances in numerical mesh
ε	dissipation rate of turbulence kinetic energy, Eq.(7)
ε_{ij}	turbulent dissipation-rate term of Reynolds stress model, Eq. (A5)
η	dimensionless strain invariant $\left(=k\sqrt{2S_{ij}S_{ij}}\Big/\varepsilon\right)$
θ	circumferential coordinate
κ	von Karman constant in the law of the wall, Eq. (17b)
ν	kinematic viscosity
ν_t	turbulent viscosity $\left(=C_\mu k^2/\varepsilon\right)$

Π_{ij}	pressure strain-rate term of Reynolds stress model
ρ	fluid density
σ_k, σ_ε	turbulent Prandtl numbers for k and ε
τ_{ij}	turbulent Reynolds stresses tensor, $\left(=-\rho\overline{u_i u_j}\right)$
τ_w	wall shear stress

Subscripts

min	refers to the minimum value
o	refers to free-stream conditions
opt	refers to the optimum value

REFERENCES

1. Eiffel, G., "*The Resistance of the Air and Aviation*," Constable and Co., London, 1913.

2. Roshko, A. and Koenig, K., "Interaction Effects on the Drag of Bluff Bodies in Tandem," *Proceedings of the Symposium on Aerodynamic Drag Mechanisms*, Ed. G. Sovran, T. Morel and W. T. Mason, Jr., Plenum Press, New York, 1978.

3. Morel, T. and Bohn, M., "Flow Over Two Circular Disks in Tandem," *ASME J. of Fluids Engineering*, Vol. 102, pp. 104 – 111, 1980.

4. Selim, M. A., "Structure of Turbulent Wakes behind Bluff Bodies," Ph. D. Thesis, Ain Shams University, 1998.

5. Launder, B. E. and Spalding, D. B., "The Numerical Computation of Turbulent Flow," *Comp. Meths. Appl. Mech. Engng.*, Vol. 3, pp. 269-289, 1974.

6. Yakhot, V., Orszag, S. A., Thangam, S., Gatski, T. B. and Speziale, C. G., "Development of Turbulence Models for Shear Flows by a Double Expansion Technique," *Phys. Fluids*, Part A, Vol. 4, pp. 1510-1520, 1992.

7. Yakhot, V. and Smith, L. M., "The Renormalization Group, the ε-Expansion and Derivation of Turbulence Models," *J. Sci. Comput*., Vol. 7, pp. 35-61, 1992.

8. Gatski, T. B., "Turbulent Flows: Model Equations and Solution Methodology," In *Handbook of Computational Fluid Mechanics*, pp. 339 - 415, Academic Press Ltd., 1996.

9. Launder, B. E., "Second-Moment Closure: Present and Future?" *Inter. J. Heat Fluid Flow*, Vol. 10, No. 4, pp. 282-300, 1989.

10. Lien, F. S. and Leschziner, M. A., "Assessment of Turbulent Transport Models Including Non-Linear RNG Eddy-Viscosity Formulation and Second-Moment Closure," *Computers and Fluids*, Vol. 23, No. 8, pp. 983-1004, 1994.

11. Cebeci, T., Khalil, E. E. and Whitelaw, J. H., "Calculation of Separated Boundary-Layer Flows," *AIAA J.*, Vol. 17, No. 12, pp.1291 - 1292, 1979.

12. Patankar, S. V., "Elliptic Systems: Finite Difference Method I," In *Handbook of Numerical Heat Transfer*, pp. 215 - 240, John Wiley & Sons, Inc., 1988.

13. Piquet, J., *Turbulent Flows Models and Physics*, Springer-Verlag Berlin Heidelberg, 1999.

14. Maskell, E. C., "A Theory of the Blockage Effects on Bluff Bodies and Stalled Wings in a Closed Wind Tunnel," *A. R. C. R & M 3400*, Nov. 1963.

15. Fail, R., Lawford, J. A. and Eyre, R. C. W., "Low Speed Experiments on the Wake Characteristics of Flat Plates Normal to an Air Stream," *A. R. C. R & M 3120*, June 1957.

16. Blevins, R. D., *Applied Fluid Dynamics Handbook*, Van Nostrand Reinhold Company Inc., 1984.

17. Hughes, W. F. and Brighton, J. A., *Theory and Problems of Fluid Dynamics*, Schaum's Outline Series, McGraw-Hill, Inc., 1991.

APPENDIX A

In the following, referring to Piquet [13], the full Reynolds-stress-model equations are given in the case of incompressible, steady, swirl-free and axisymmetric flow in cylindrical coordinates.

$$U\frac{\partial\overline{u^2}}{\partial x}+V\frac{\partial\overline{u^2}}{\partial r}=-2\left(\overline{u^2}\frac{\partial U}{\partial x}+\overline{uv}\frac{\partial U}{\partial r}\right)+\frac{2}{\rho}\overline{p\frac{\partial u}{\partial x}}-\left[\frac{\partial\overline{u^3}}{\partial x}+\frac{1}{r}\frac{\partial(r\overline{vu^2})}{\partial r}+\frac{2}{\rho}\frac{\partial\overline{pu}}{\partial x}\right]$$
$$+\nu\left[\frac{\partial^2\overline{u^2}}{\partial x^2}+\frac{1}{r}\frac{\partial}{\partial r}\left(r\frac{\partial\overline{u^2}}{\partial r}\right)\right]-\varepsilon_{xx} \tag{A1}$$

$$U\frac{\partial\overline{v^2}}{\partial x}+V\frac{\partial\overline{v^2}}{\partial r}=-2\left(\overline{uv}\frac{\partial V}{\partial x}+\overline{v^2}\frac{\partial V}{\partial r}\right)+\frac{2}{\rho}\overline{p\frac{\partial v}{\partial r}}-\left[\frac{\partial\overline{uv^2}}{\partial x}+\frac{1}{r}\frac{\partial(r\overline{v^3})}{\partial r}-2\frac{\overline{vw^2}}{r}+\frac{2}{\rho}\frac{\partial\overline{pv}}{\partial r}\right]$$
$$+\nu\left[\frac{\partial^2\overline{v^2}}{\partial x^2}+\frac{1}{r}\frac{\partial}{\partial r}\left(r\frac{\partial\overline{v^2}}{\partial r}\right)-2\frac{\overline{v^2}}{r^2}\right]-\varepsilon_{rr} \tag{A2}$$

$$U\frac{\partial\overline{w^2}}{\partial x}+V\frac{\partial\overline{w^2}}{\partial r}=-2\overline{w^2}\frac{V}{r}-\left[\frac{\partial\overline{uw^2}}{\partial x}+\frac{1}{r}\frac{\partial(r\overline{vw^2})}{\partial r}+2\frac{\overline{vw^2}}{r}\right]$$
$$+\nu\left[\frac{\partial^2\overline{w^2}}{\partial x^2}+\frac{1}{r}\frac{\partial}{\partial r}\left(r\frac{\partial\overline{w^2}}{\partial r}\right)-2\frac{\overline{w^2}}{r^2}\right]-\varepsilon_{\theta\theta} \tag{A3}$$

$$U\frac{\partial\overline{uv}}{\partial x}+V\frac{\partial\overline{uv}}{\partial r}=-\overline{u^2}\frac{\partial V}{\partial x}-\overline{uv}\left(\frac{\partial U}{\partial r}+\frac{\partial V}{\partial x}\right)-\overline{v^2}\frac{\partial U}{\partial r}+\overline{\frac{p}{\rho}\left(\frac{\partial u}{\partial r}+\frac{\partial v}{\partial x}\right)}$$
$$-\left[\frac{\partial\overline{u^2v}}{\partial x}+\frac{1}{r}\frac{\partial(r\overline{uv^2})}{\partial r}-\frac{\overline{uw^2}}{r}+\frac{1}{\rho}\left(\frac{\partial\overline{pu}}{\partial r}+\frac{\partial\overline{pv}}{\partial x}\right)\right]+\nu\left[\frac{\partial^2\overline{uv}}{\partial x^2}+\frac{\partial}{\partial r}\left(\frac{1}{r}\frac{\partial(r\overline{uv})}{\partial r}\right)\right]-\varepsilon_{xr} \tag{A4}$$

Where the right–hand side terms are identified, respectively, as the turbulent production, the pressure strain rate, the turbulent diffusion, the molecular diffusion and the turbulent dissipation rate defined as follows:

$$\varepsilon_{ij}=2\nu\overline{\frac{\partial u_i}{\partial x_m}\frac{\partial u_j}{\partial x_m}} \tag{A5}$$

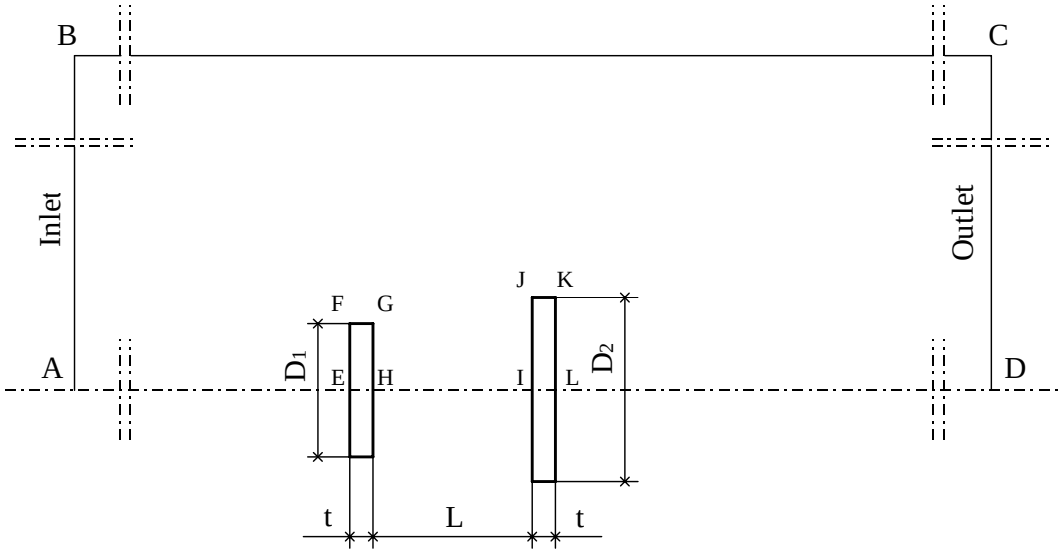

Fig.1: The flow geometry and computational domain.

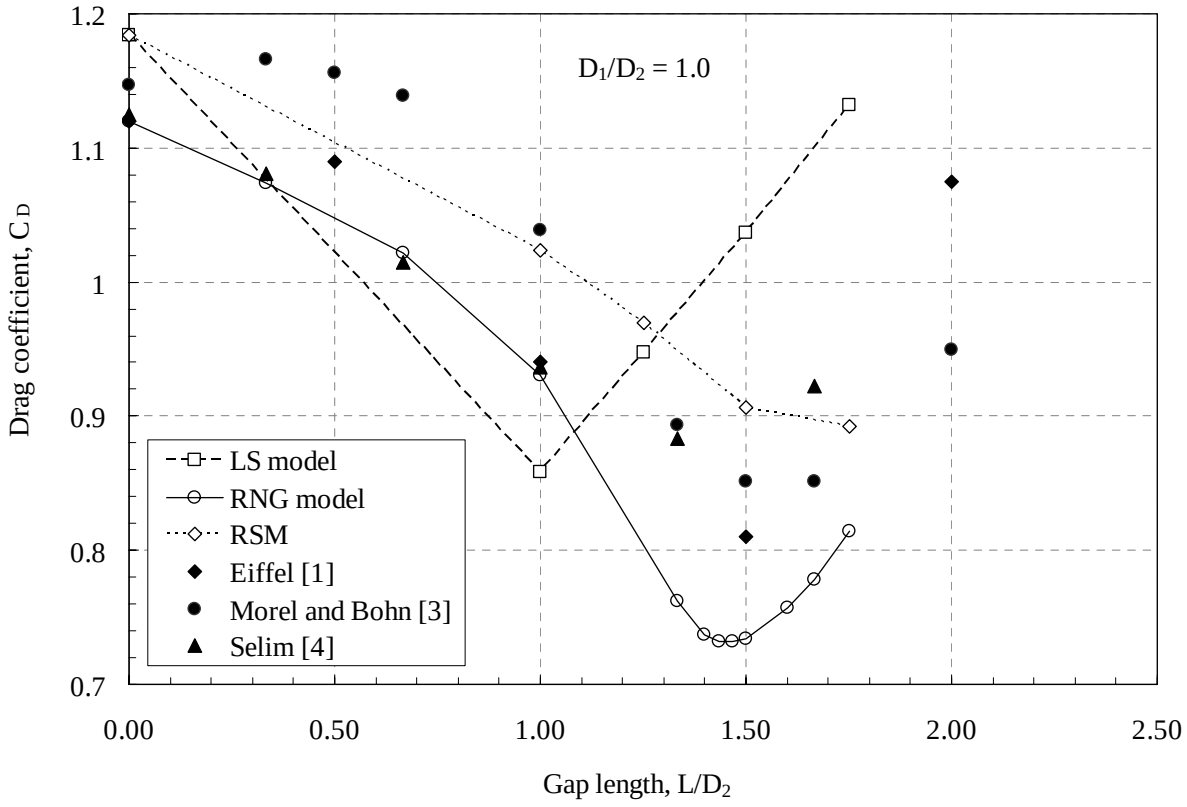

Fig. 2: Variation of the drag coefficient with the gap length as obtained using three different turbulence models.

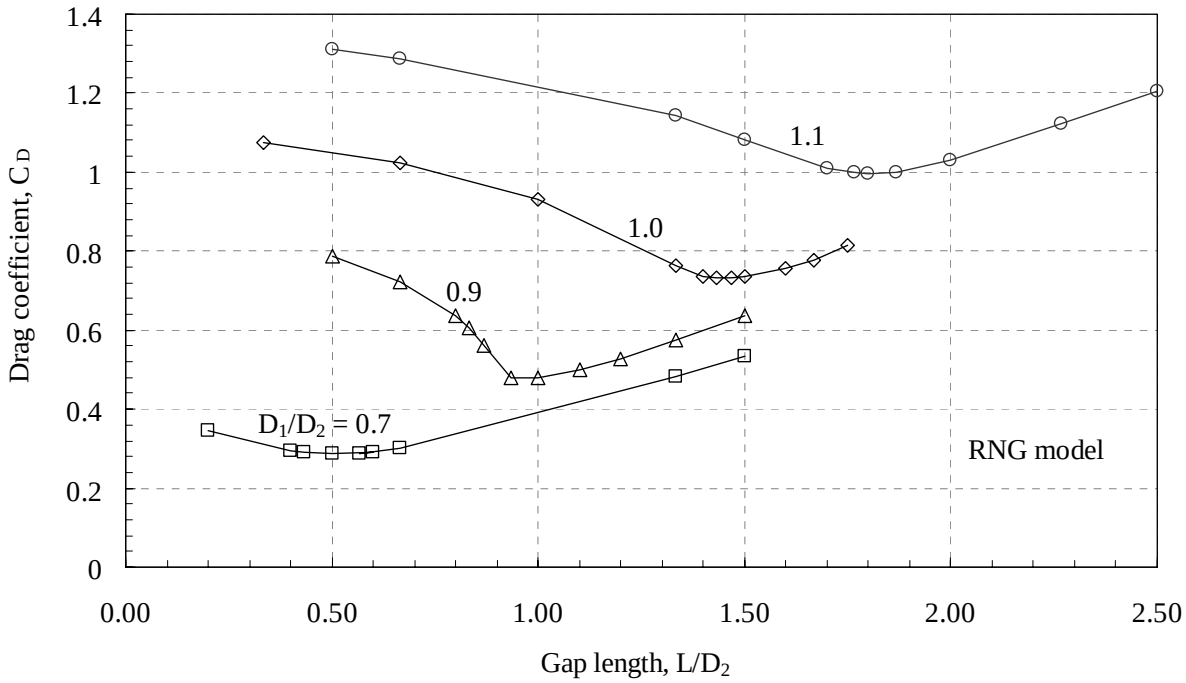

Fig. 3: Variation of the drag coefficient with the gap length for different diameters ratios.

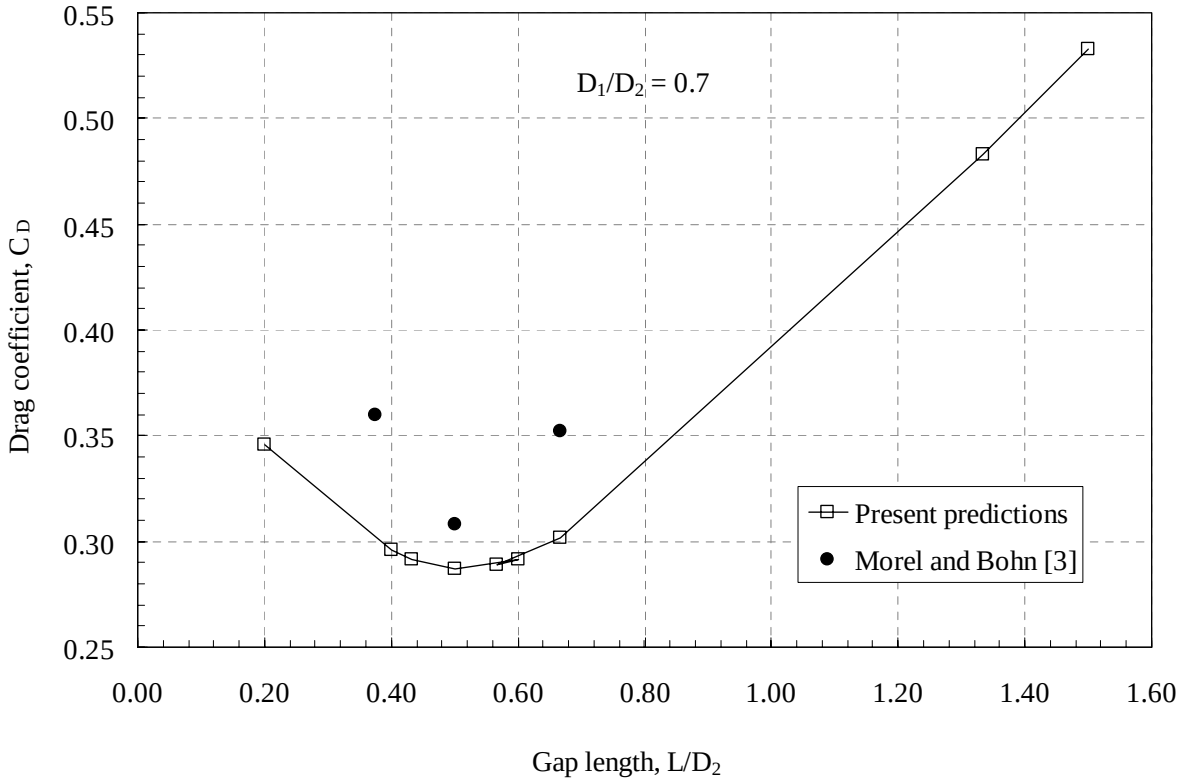

Fig. 4: Variation of the drag coefficient with the gap length for as compared with the experimental results of Morel and Bohn [3].

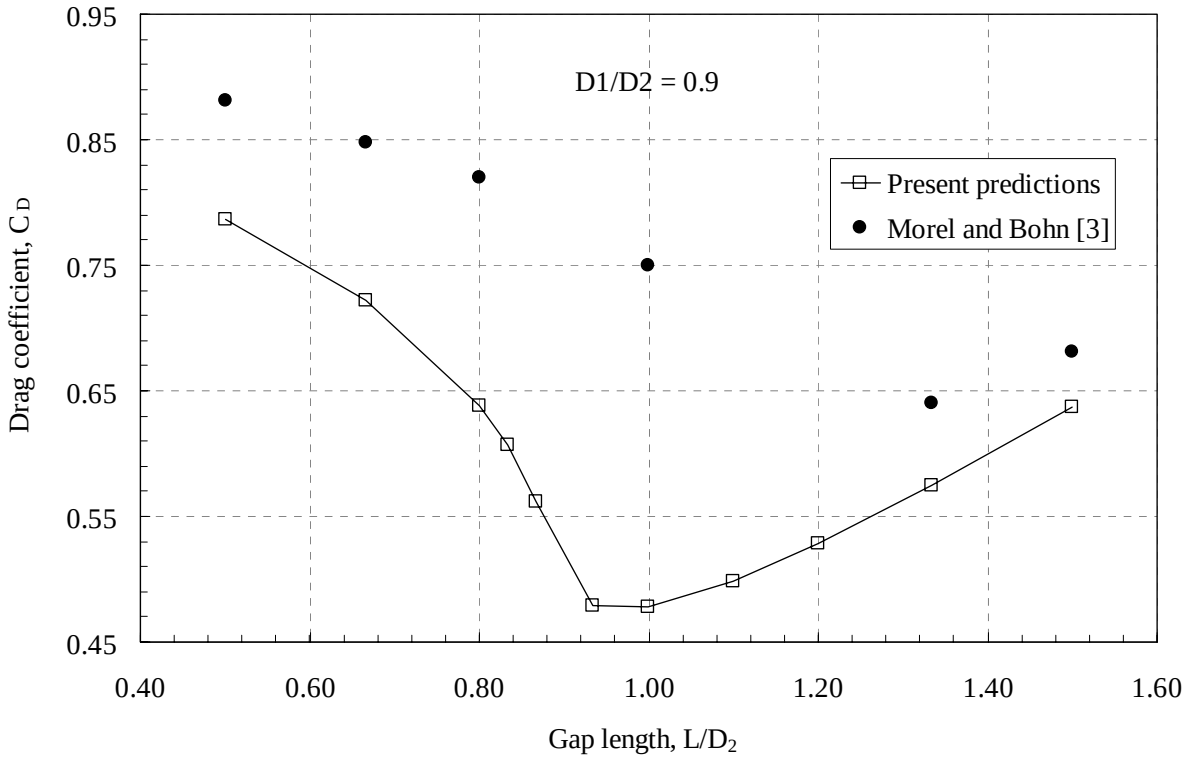

Fig. 5: Variation of the drag coefficient with the gap length for as compared with the experimental results of Morel and Bohn [3].

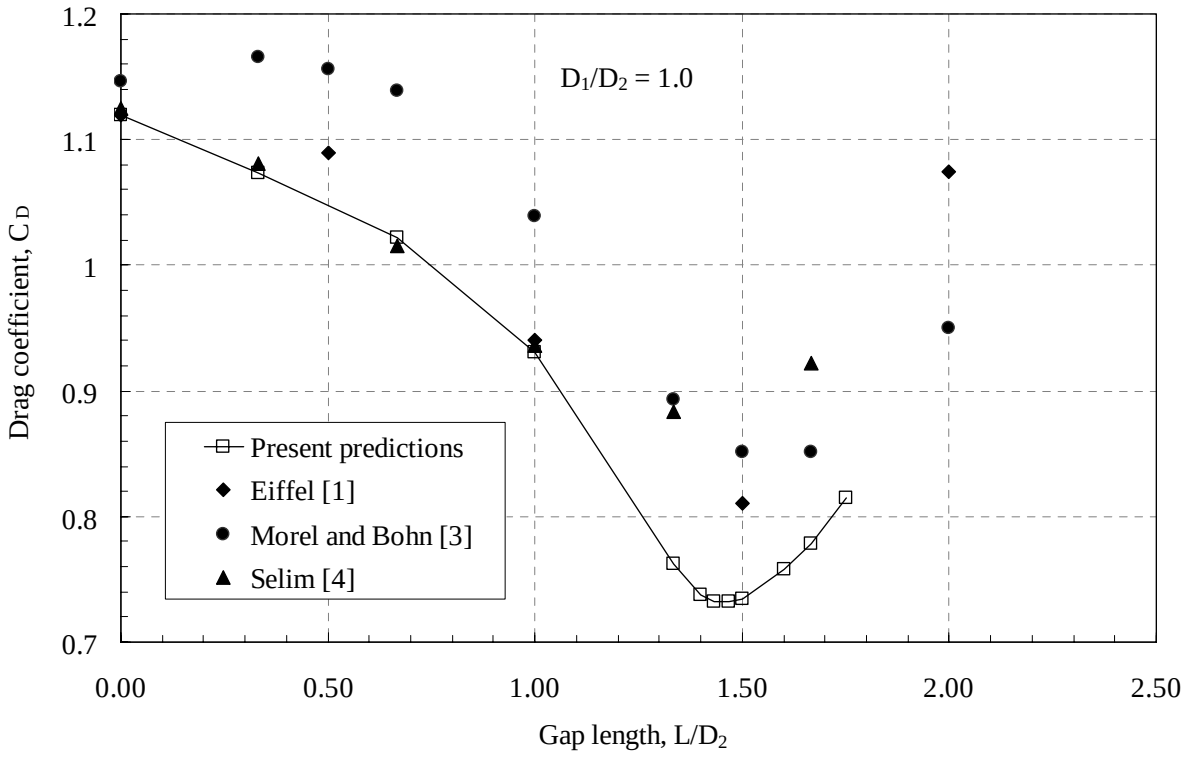

Fig. 6: Variation of the drag coefficient with the gap length for as compared with the experimental results of refs. [1, 3 and 4].

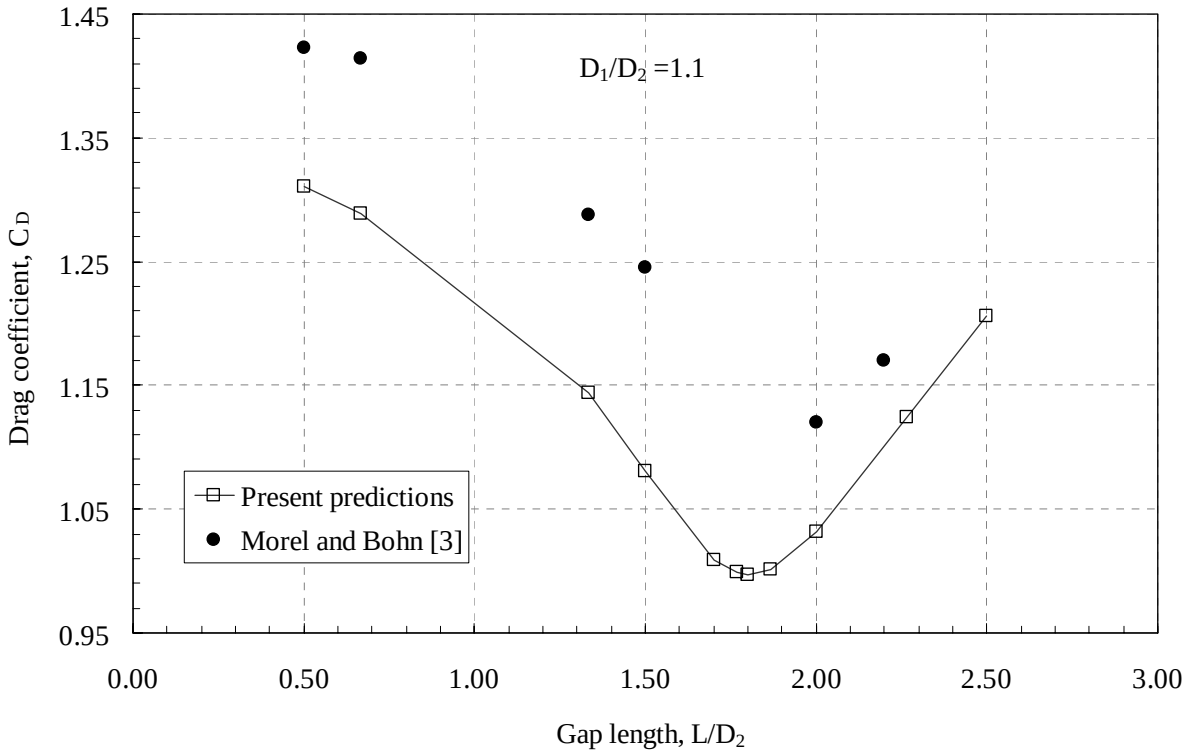

Fig. 7: Variation of the drag coefficient with the gap length for as compared with the experimental results of Morel and Bohn [3].

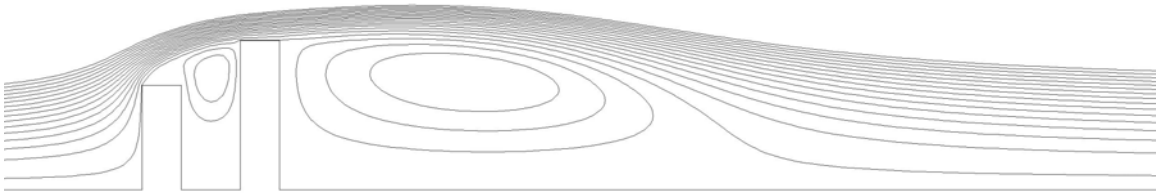

a) $L/D_2 = 0.2$ and $C_D = 0.346$

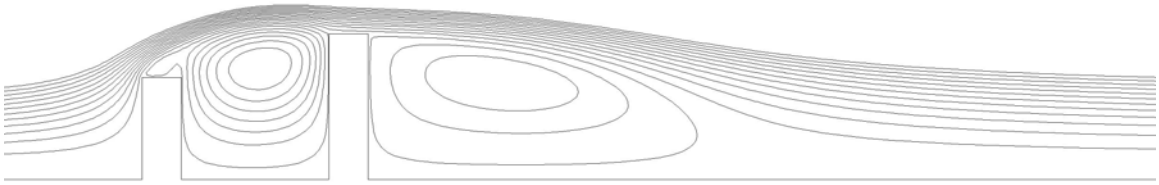

b) $L/D_2 = 0.5$ and $C_D = 0.287$

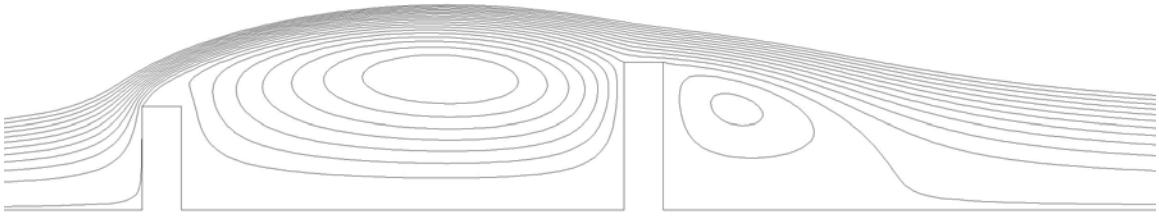

c) $L/D_2 = 1.5$ and $C_D = 0.533$

Fig. 8: Mean streamline representation for tandem configuration with $D_1/D_2 = 0.7$.

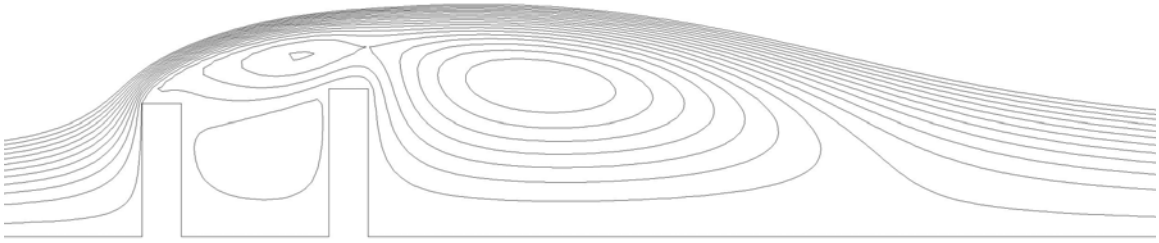

a) $L/D_2 = 0.5$ and $C_D = 0.787$

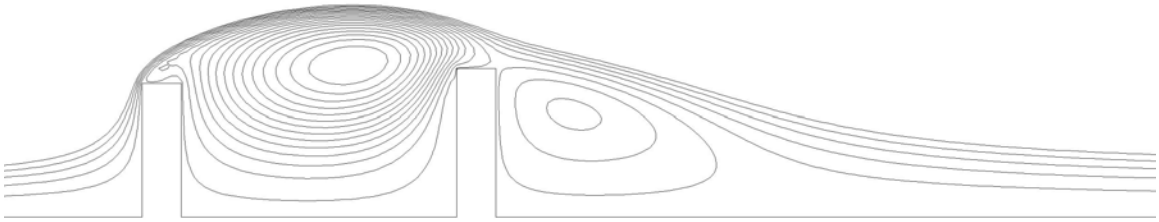

b) $L/D_2 = 0.93$ and $C_D = 0.479$

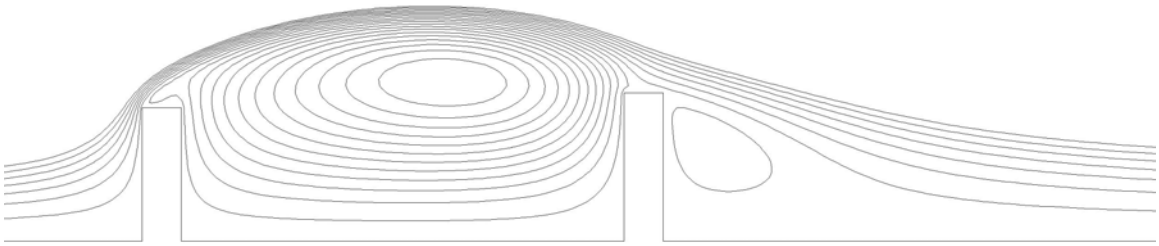

c) $L/D_2 = 1.5$ and $C_D = 0.637$

Fig. 9: Mean streamline representation for tandem configuration with $D_1/D_2 = 0.9$.

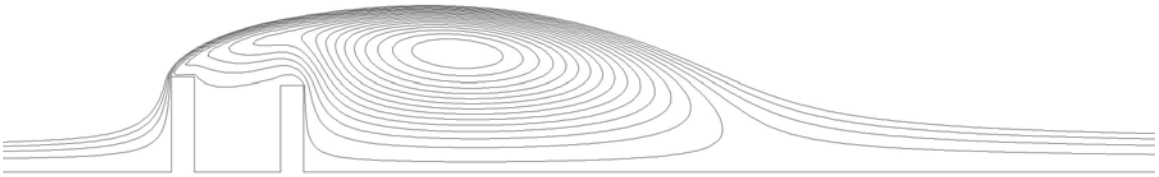

a) $L/D_2 = 0.5$ and $C_D = 1.31$

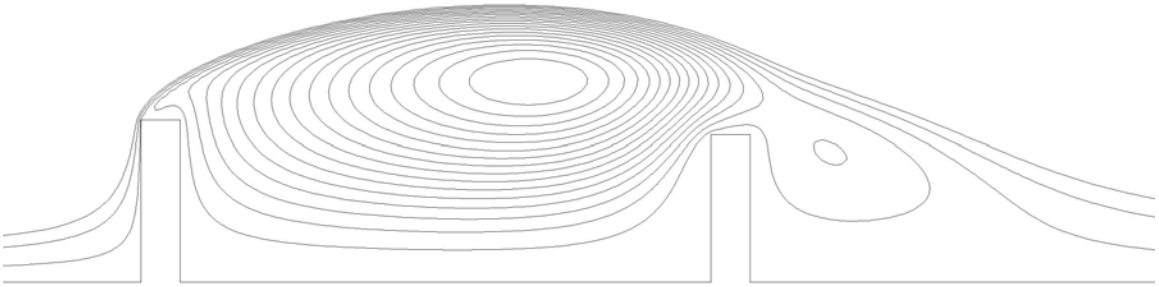

b) $L/D_2 = 1.8$ and $C_D = 0.997$

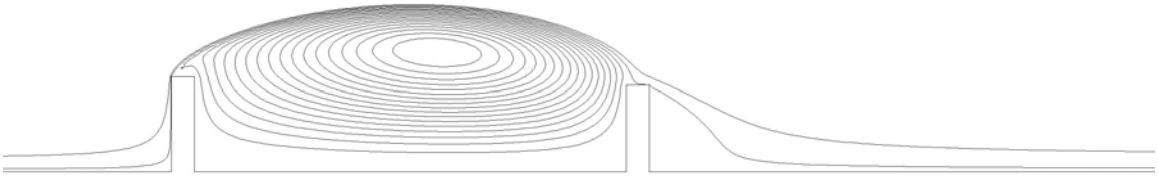

c) $L/D_2 = 2.5$ and $C_D = 1.206$

Fig. 10: Mean streamline representation for tandem configuration with $D_1/D_2 = 1.1$.